Patient-Adaptive Lesion Metabolism Analysis by Dynamic PET Images

Fei Gao[1], Huafeng Liu[2,1], and Pengcheng Shi[1]

[1] Golisano College of Computing and Information Sciences, Rochester Institute of Technology, Rochester, NY, 14623, USA
[2] State Key Laboratory of Modern Optical Instrumentation, Zhejiang University, Hangzhou, 310027, China

Abstract. Dynamic PET imaging provides important spatial-temporal information for metabolism analysis of organs and tissues, and generates a great reference for clinical diagnosis and pharmacokinetic analysis. Due to poor statistical properties of the measurement data in low count dynamic PET acquisition and disturbances from surrounding tissues, identifying small lesions inside the human body is still a challenging issue. The uncertainties in estimating the arterial input function will also limit the accuracy and reliability of the metabolism analysis of lesions. Furthermore, the sizes of the patients and the motions during PET acquisition will yield mismatch against general purpose reconstruction system matrix, this will also affect the quantitative accuracy of metabolism analyses of lesions. In this paper, we present a dynamic PET metabolism analysis framework by defining a patient adaptive system matrix to improve the lesion metabolism analysis. Both patient size information and potential small lesions are incorporated by simulations of phantoms of different sizes and individual point source responses. The new framework improves the quantitative accuracy of lesion metabolism analysis, and makes the lesion identification more precisely. The requirement of accurate input functions is also reduced. Experiments are conducted on Monte Carlo simulated data set for quantitative analysis and validation, and on real patient scans for assessment of clinical potential.

1 Introduction

Dynamic Positron Emission Tomography (dPET) is a molecular imaging technique that is used to monitor the spatiotemporal distribution of a radiotracer *in vivo* and enables cellular level metabolism analysis in clinical routine. dPET provides a good promise for quantitative lesion metabolism analysis to help identify lesions. However, due to poor statistical properties of the measurement data in low count dynamic PET acquisition and disturbances from surrounding tissues, identifying small lesions inside the human body is still a challenging issue. Furthermore, the mismatch between general purpose models and patient size/motions makes the situation even worse.

Quantitative kinetic analysis of radiotracer uptakes requires the reconstruction of kinetic parameters[1–3]. The mainstream is statistical reconstruction algorithms, however, whose quality is determined by the accuracy of sophisticated

system probability matrix (SM). Many efforts have been devoted to improve the accuracy of SM [4–7]. However, the ideal SM is almost impossible to obtain under practical conditions. The general purpose SM also could not compensate different sizes of patients and the motions during acquisition, which will decrease the accuracy of reconstructions. Furthermore, the reconstruction of dynamic PET image sequences, whose poor temporal resolution, insufficient photon counts, more complicated data corrections and poor statistical properties of measurement data also requires a more accurate SM.

In this paper, we present a dynamic PET metabolism analysis framework by defining a patient adaptive system matrix to improve the lesion metabolism analysis. Both patient size information and potential small lesion information are incorporated by simulations of phantoms of different sizes and individual point source responses[8–10]. Experiments of 90 studies are conducted using 15 phantoms of different sizes based on Zubal thorax phantom. Each experiment has randomly generated motions and a lesions in lung. Both true lesion and false lesion cases are studies. We also analyze the results using input functions of different accuracies. Our method shows obvious improvements in identifying lesions (including sizes, true/false situations, metabolism rates), and reduces the requirement of the accuracy of input functions. An experiment based on real patient scans is also conducted for assessment of clinical potential.

2   Method

2.1   Tracer Kinetics

Dynamic PET imaging provides the opportunities to perform lesion metabolism analysis by using compartmental models to quantitatively describe regional radiotracer kinetics. A typical three compartmental model (Phelps 4K model) can be mathematically represented by a set of ordinary differential equations [11].

$$\frac{dC_F(t)}{dt} = k_1(t)C_P(t) + k_4(t)C_B(t) - (k_2(t) + k_3(t))C_F(t) \tag{1}$$

$$\frac{dC_B(t)}{dt} = k_3(t)C_F(t) - k_4(t)C_B(t) \tag{2}$$

where C_P(pmol/ml) is arterial concentration of injected radiotracer, C_F is the free and non–specific binding ligands, C_B is the specific binding tracers in tissues. Parameters k_1, k_2, k_3 and $k_4(min^{-1})$ are first-order rate constants specifying radiotracer transport rates. The general PET measurement equation is $Y = DX + e$. With the compartment model introduced, the activity distribution X should be the combination of C_F, C_B, C_P and fractional volume of blood f_v

$$X(t) = (1 - f_v)(C_F(t) + C_B(t)) + f_vC_P(t) \tag{3}$$

C_F, C_B are the functions of kinetic parameters, if defining $\kappa = \{k_1, k_2, k_3, k_4\}$

$$Y(t) = DX(\kappa, t) + e(t) \tag{4}$$

2.2   System Matrix Derived from Supervised Learning

Statistical reconstruction requires a well modeled SM, which directly determines the accuracy of reconstruction results. The SM D is extended to include 2 parts, D_1 is a SM generated from geometry information and physical phenomena, and will account for sizes and motions of different patients, D_2 is an additional SM generated from point source responses. D_1 and D_2 are full size SM, and combined together by weighting matrices w_1 and w_2 according to the anatomical information of patients. This effort makes the SM more patient adaptive. The measurement equation is extended from Eqn.4 to be

$$Y(t) = \begin{bmatrix} w_1 & w_2 \end{bmatrix} \begin{bmatrix} D_1 \\ D_2 \end{bmatrix} X(\kappa, t) + e(t) \tag{5}$$

w_1, w_2, D_1, D_2 are updated by supervised learning. Training sets are provided by Monte Carlo simulations using GATE toolbox. Correspondingly, 2 series of simulations are performed, one is performed with human thorax phantom of different sizes, and the other is done by point source response inside a thorax phantom of normal size. Denoting the activity concentrations as $X = \{x_1, x_2, \cdots x_n\}$ and measurement datasets as $Y = \{y_1, y_2, \cdots x_n\}$. n is the number of training sets, and every dataset is a dynamic data sequence related to time t. For simplification of expression, Eqn.5 is written as $Y(t) = D'X(k, t) + e(t)$. Since ADALINE has been proved to be simple yet successful for updating SM in[7], we also adopt ADALINE for our SM training here. The initialization of D_1 and D_2 are the SMs generated with uniform cylindrical phantom. The update procedure by ADALINE using back-propagation and least mean square error is:

$$\hat{y}_m(t) = D'_m X(k, t) + e_m(t) \qquad \delta_k(t) = Y(t) - \hat{y}_m(t) \tag{6}$$
$$D'_{m+1}(t) = D'_m(t) + 2L\delta_m X^T(t) \qquad e_{m+1}(t) = e_m(t) + 2L\delta_m(t) \tag{7}$$

where m is the iteration step of training, and L is the learning rate. After defining a precision level of learning ϵ,

$$D' \qquad \textbf{subject to} \qquad \begin{cases} Y(t) - \hat{y}_m(t) < \epsilon \\ \hat{y}_m(t) - Y(t) < \epsilon \end{cases} \tag{8}$$

the weighting matrices w_1 and w_2 will be obtained when convergence is achieved.

2.3   Parameter Reconstruction of Dynamic PET

The kinetic model and image reconstruction are combined in one equation, the log likelihood function can be derived with measurement data $y(t)$ as

$$\mathcal{L}(y|\kappa) = \sum_t y(t) \log \bar{y}(\kappa, t) - \bar{y}(\kappa, t) \tag{9}$$

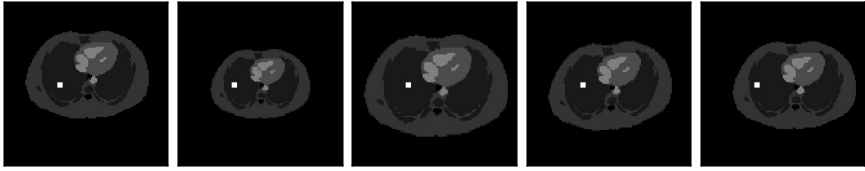$$\textbf{where} \quad \bar{y}(\kappa, t) = D'x(\kappa, t) + e(t) \tag{10}$$

Fig. 1. First 5 phantoms
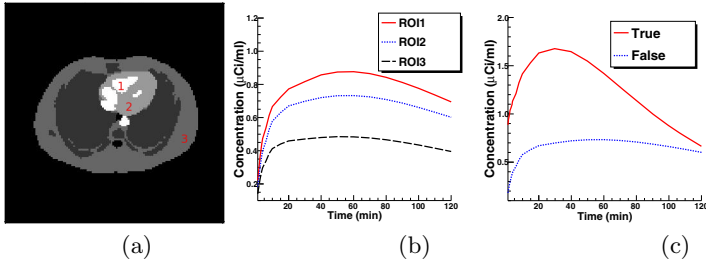

(a)   (b)   (c)

Fig. 2. (a) Standard Zubal Phantom; (b) TAC curves of 3 ROIs indicated in (a); (c) TAC curves of true lesion and false lesion

$$\hat{\kappa} = \arg\max \Phi(\kappa), \qquad \Phi(\kappa) = \mathcal{L}(y|k) - \beta \mathcal{U}(k). \tag{11}$$

where $\mathcal{U}$ is the penalty regularization term with parameter β controlling resolution/noise tradeoff. Eqn.11 is solved by a paraboloidal surrogates algorithm in [12]. Since the parameter reconstruction has a higher data dimensionality/freedom, we also define the evaluation of a student's t-distribution hypothesis test to determine their statistical differences among iterations. By selecting Region of Interest (ROI), calculate $t = \frac{|\bar{x}_m - \bar{x}_{m+1}|}{\sigma}$, where $\sigma = (\frac{var_m + var_{m+1} - 2cov_{m,m+1}}{N})^{0.5}$ and $cov_{m,m+1} = \frac{1}{N-1}\sum_{i=1}^{N}(x_{m,i} - \bar{x}_m)(x_{m+1,i} - \bar{x}_{m+1})$. $\bar{x}_m$ and $\bar{x}_{m+1}$ are the means in ROI at iteration m and $m+1$, var is the corresponding variances across the image elements. cov is the covariance across the two iterations. t is calculated until less than $t_{0.05}$ in the t-table to show a confidence level of 95% that the difference between images is small enough.

3   Experiment and Results

3.1   Monte Carlo Simulated Dynamic PET Data

Experiment Settings. First dataset is generated using Monte Carlo simulations of the acquisition of our PET scanner. There are totally 90 studies.

1. A series of 15 phantoms is generated based on Zubal thorax phantom of different sizes (to represent different patients from skinny to fat). Randomly generated motions (shifts and rotation) are added to each phantom.

Table 1. Kinetic parameters used for Monte Carlo simulations

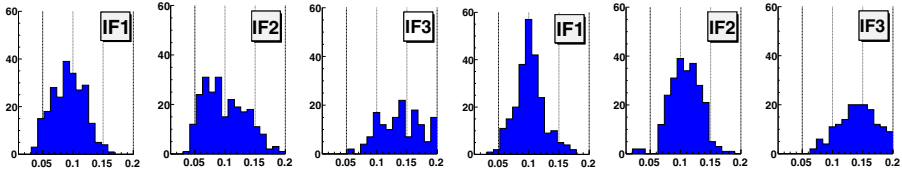| ROI1				ROI2			
k1	k2	k3	k4	k1	k2	k3	k4
0.102	0.130	0.062	0.0068	0.082	0.102	0.045	0.0041
ROI3				Lesion			
k1	k2	k3	k4	k1	k2	k3	k4
0.064	0.124	0.042	0.0035	0.4870	0.7120	0.1950	0.0341

Fig. 3. Influx rates by General Method (left 3) and Our Method (right 3)

2. A lesion is added in every phantom. For each lesion, 2 cases are studied: true lesion (e.g. tumor) and false lesion (e.g. some normal tissue with undesired radiotracer concentration.). First 5 phantoms with lesions are shown in Fig.1.

3. The Time Activity Curves (TAC) are generated by Feng input, $C_P^{FDG}(t) = (A_1t - A_2 - A_3)e^{-\lambda_1 t} + A_2e^{-\lambda_2 t} + A_3e^{-\lambda_3 t}$. The values of the parameters λ_i and A_i selected here are $A_1 = 28\mu Ci/mL/min$, $A_2 = 0.75\mu Ci/mL$, $A_3 = 0.70\mu Ci/mL$, $\lambda_1 = 4.1339min^{-1}$, $\lambda_2 = 0.01043min^{-1}$ and $\lambda_3 = 0.1191min^{-1}$. For Feng input, the final results need be calibrated for possible underestimation. The dynamic acquisition consists of 29 frames: $6\times5sec$, $2\times15sec$, $6\times0.5min$, $3\times2min$, $2\times5min$ and $10\times10min$. The kinetic parameters used in simulations are listed in Table. 1. The TACs of 3 normal ROIs are shown in Fig. 2 (b) and TACs of true lesion and false lesion are shown in Fig. 2 (c). False lesion uses the same kinetic parameters as ROI2.

4. All the parameter reconstructions are performed with 3 different input function initializations: Input Function 1 is perfect input function (equivalent to perfect blood sampling with less than 5% error), Input Function 2 is good input function (equivalent to a disturbed blood sampling with about 20% error), Input Function 3 is an Image Derived Input Function (IDIF). In next part, reconstructions with general purpose SM are called General Method.

Experiment Results. The influx rate maps are calculated based on **Influx Rate** $= \frac{k_1 k_3}{k_2 + k_3}$ to evaluate the reconstruction results.

First, all the true lesions are extracted from 45 studies and analyzed pixel-wisely. Fig.3 shows the histograms of influx rates of lesions calculated by results from General Method and Our Method using different input functions. When using Input Function 1 and Input Function 2, our results are closer to the true value (it is 0.1047), and show obvious smaller standard derivations, which will help identify lesion sizes more precisely. With Input Function 3, the bad
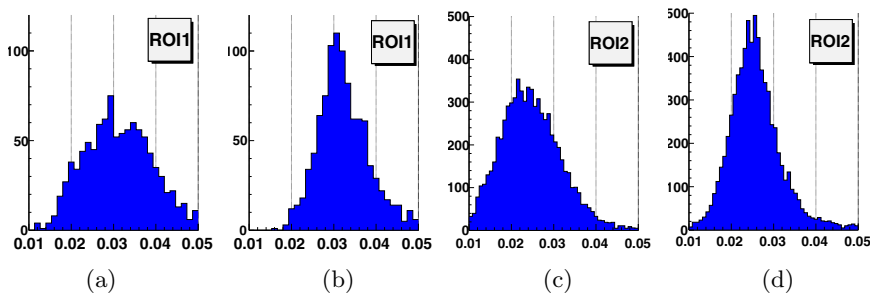
Fig. 4. Histograms of influx rate by (a) General Method in ROI1; (b) Our Method in ROI1; (c) General Method in ROI2; (d) Our Method in ROI2

estimation of input function leads to the overestimation of influx rates, however, our method still has more pixels near the true value. Our Method also introduces improvements in other regions. For ROI 1 and 2 indicated by Fig.2 (a), in Fig.4 we show the histograms of influx rates from all the pixels of all studies in corresponding ROIs. As the lesion region, results from our method are closer to the true values with obviously smaller standard derivations.

Fig.5 shows the influx rate maps of Phantom 3 using Input Function 2. This special case is to represents the oversized patient with underestimations of the lesion. Our method first shows a better overall image quality. Then our method also show smoother results and better discrimination of lesion region and different ROIs like indicated by histograms in Fig.3 and Fig.4. The lesions are more clear and uniform by our method, and especially the false lesion is identified clearly to metabolize like muscles.

We summarize all 90 studies in Table.2, which shows the ratio of successful identification of lesions using different input functions ("Success" means the difference between mean of lesion region and true value should be less than 40%, which is just the value to separate lesions from muscles in our experiments when lesions are near body surface or heart, and the standard deviations of lesion regions should be less than 0.67 to correctly identify the sizes of lesions). Both methods performs well by using Input Function 1 (perfect input function). However, with Input Function 2 (with disturbances), the accuracy of General Method decreases, but our method still provides good results. The simulation results show the improvement in identifying lesions by our method, and the reduction of requirement of accurate input function.

3.2   Real Patient Experiments

The real patient data in this study was a dynamic PET scan acquired from a 28-year-old, 75kg male volunteer using our PET scanner. 10 mCi ^{18}F-FDG was injected and a dynamic acquisition of the thoracic cavity started just after injection. The acquisition consists of 40 time frames: $20\times0.5min$, $15\times1min$, and $5\times2min$. All corrections are performed properly with the software provided by the scanner. The input function is estimated by the image-derived method. Fig. 6
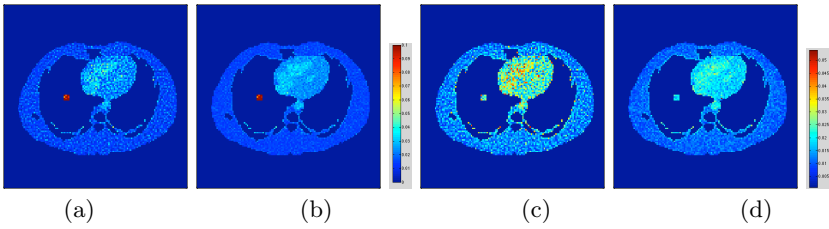
(a)   (b)   (c)   (d)

Fig. 5. Influx rate maps of Phantom 3. (a) General Method with true lesion; (b) Our Method with true lesion; (c) General Method with false lesion; (d) Our Method with false lesion.

Table 2. Summary of experiments

	Group1	Group2	Group3	Group4	Group5	Group6
Lesion Type	True	True	True	False	False	False
Input Function	1	2	3	1	2	3

Successful Estimation/Total Studies	Group1	Group2	Group3	Group4	Group5	Group6
General Mehtod	13/15	7/15	5/15	11/15	7/15	6/15
Our Mehtod	14/15	13/15	7/15	12/15	12/15	7/15

Muscles	0.0054
Our Method	0.0071
General Method	0.0085

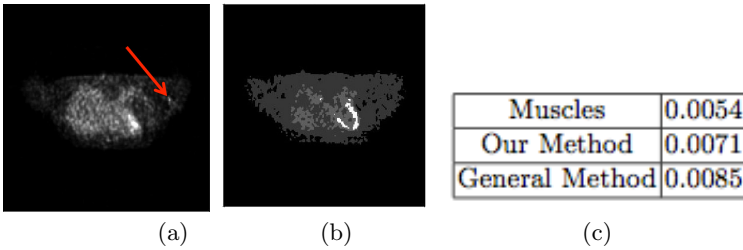(a)   (b)   (c)

Fig. 6. (a) Lesion in 40th slice; (b) 32nd slice; (c) Influx rates

(a) shows a lesion region by a red arrow in the 40th slice. We calculate the influx rates of the lesion and compare them with the heart muscles in the 32nd slice. The lesion metabolism calculated by our method is closer to the muscles than that by General Method, and the lesion is confirmed by the doctor as a false lesion with temporarily increased metabolism than muscles, results from our method show potential improvement in diagnosis.

4   Conclusion

We presented a dynamic PET metabolism analysis framework by defining a patient adaptive SM. Experiment results show obvious improvements on identifying lesions by our method, and requirement of input functions is also reduced.

References

1. Rahmim, A., Tang, J., Zaidi, H.: Four-Dimensional (4D) Image Reconstruction Strategies in Dynamic PET: Beyond Conventional Independent Frame Reconstruction. Medical Physics 36(8), 3654 (2009)
2. Wang, G., Qi, J.: Generalized Algorithms for Direct Reconstruction of Parametric Images From Dynamic PET Data. IEEE Transactions on Medical Imaging 28(11), 1717–1726 (2009)
3. Gao, F., Liu, H., Shi, P.: Robust Estimation of Kinetic Parameters in Dynamic PET Imaging. In: Fichtinger, G., Martel, A., Peters, T. (eds.) MICCAI 2011, Part I. LNCS, vol. 6891, pp. 492–499. Springer, Heidelberg (2011)
4. Moehrs, S., Defrise, M., Belcari, N., Guerra, A.D., Bartoli, A., Fabbri, S., Zanetti, G.: Multi-Ray-Based System Matrix Generation for 3D PET Reconstruction. Physics in Medicine and Biology 53(23), 6925 (2008)
5. Panin, V., Kehren, F., Rothfuss, H., Hu, D., Michel, C., Casey, M.: PET Reconstruction with System Matrix Derived from Point Source Measurements. IEEE Transactions on Nuclear Science 53(1), 152–159 (2006)
6. Zhang, L., Staelens, S., Holen, R.V., Beenhouwer, J.D., Verhaeghe, J., Kawrakow, I., Vandenberghe, S.: Fast and Memory-Efficient Monte Carlo-Based Image Reconstruction for Whole-Body PET. Medical Physics 37(7), 3667 (2010)
7. Su, K.H., Wu, L.C., Lee, J.S., Liu, R.S., Chen, J.C.: A Novel Method to Improve Image Quality for 2-D Small Animal PET Reconstruction by Correcting a Monte Carlo-Simulated System Matrix Using an Artificial Neural Network. IEEE Transactions on Nuclear Science 56(3), 704–714 (2009)
8. Wu, H., Pal, D.O., Sullivan, J., Tai, Y.C.: A Feasibility Study of a Prototype PET Insert Device to Convert a General-Purpose Animal PET Scanner to Higher Resolution. Journal of Nuclear Medicine 49(1), 79–87 (2008)
9. Li, Z., Li, Q., Yu, X., Conti, P., Leahy, R.: Lesion Detection in Dynamic FDG-PET Using Matched Subspace Detection. IEEE Transactions on Medical Imaging 28(2), 230–240 (2009)
10. Laffon, E., de Clermont, H., Vernejoux, J.M., Jougon, J., Marthan, R.: Feasibility of Assessing [18F]FDG Lung Metabolism with Late Dynamic PET Imaging. Molecular Imaging and Biology 13(2), 378–384 (2011)
11. Vriens, D., Visser, E.P., de Geus-Oei, L.F., Oyen, W.J.G.: Methodological Considerations in Quantification of Oncological FDG PET Studies. European Journal of Nuclear Medicine and Molecular Imaging 37(7), 1408–1425 (2010)
12. Fessler, J., Erdogan, H.: A Paraboloidal Surrogates Algorithm for Convergent Penalized-Likelihood Emission Image Reconstruction. In: Nuclear Science Symposium, Conference Record, vol. 2, pp. 1132–1135 (1998)